Supporting Information for

Simulation and Analysis of the Relaxation Pathways of a Photochromic Furylfulgide

Michał Andrzej Kochman,[*,†] Tomasz Gryber,[*,†] Bo Durbeej,[‡] and Adam Kubas[†]

[†] Institute of Physical Chemistry, Polish Academy of Sciences, Ul. Marcina Kasprzaka 44/52, 01-224 Warszawa, Poland.
[‡] Division of Theoretical Chemistry, Department of Physics, Chemistry and Biology (IFM), Linköping University, 581 83 Linköping, Sweden

e-mail: mkochman@ichf.edu.pl

Contents

S1 Benchmark Calculations

Part of the challenge in simulating the excited-state dynamics of photoactive compounds such as furylfulgides is that the large sizes of these molecules require a tradeoff between accuracy and computational efficiency. In the present study, this compromise was achieved by resorting to spin-flip time-dependent density functional theory[1,2] (SF-TDDFT) for the electronic structure component of the nonadiabatic molecular dynamics (NAMD) simulations. SF-TDDFT is a relatively new and untested method, and it could not automatically be assumed that it provides a realistic description of the ground- and excited-state potential energy surfaces (PESs) of furylfulgides. For this reason, we assessed the accuracy of the SF-TDDFT method against the benchmark provided by extended multi-state multireference second-order perturbation theory[3] (XMS-CASPT2). XMS-CASPT2 is a variant of multireference perturbation theory,[4–6] and is a widely applicable and accurate[7–9] method for the calculation of excited electronic states, making it a good choice of benchmark for SF-TDDFT.

For reasons of computational tractability, the benchmark calculations were performed for compound **2**, whose structure is shown in Figure S1. Compound **2** is a truncated computational model of a furylfulgides in the series **1** (see Figure 1 in the main body of our paper) in which all alkyl groups were replaced by hydrogen atoms. In reality, the cyclic form of compound **2** would almost certainly be highly unstable, and would rapidly undergo dehydrogenation from atoms C1 and C6, but this is irrelevant for our purposes.

The benchmark calculations were carried out by scanning the relevant PESs of

Figure S1: Isomers of the truncated model compound **2**, and the relevant photochemical reaction paths.

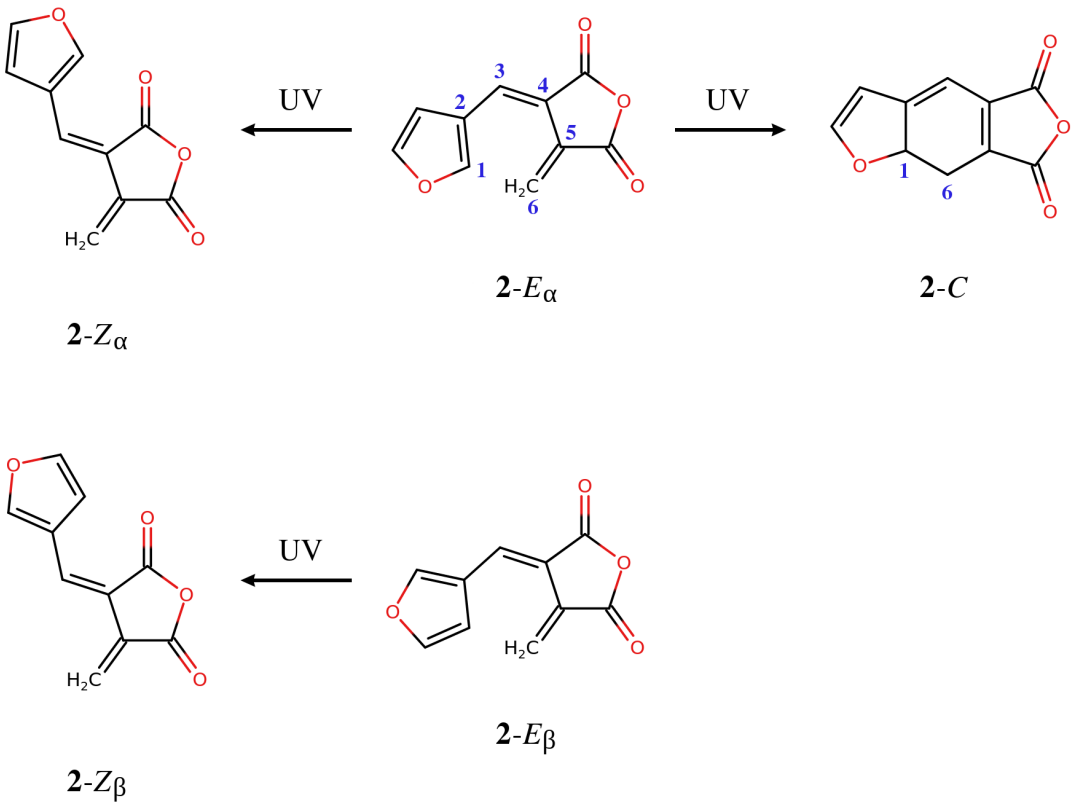

compound **2** along reaction paths for the three photochemical processes indicated in Figure S1: photocyclisation ($E_\alpha \rightarrow C$), $E_\alpha \rightarrow Z_\alpha$ photoisomerisation, and $E_\beta \rightarrow Z_\beta$ photoisomerisation. The reaction paths were generated as follows. First, the ground-state equilibrium geometries of the five relevant isomers of compound **2** were optimised at the SF-TDDFT level of theory. The parameters of these SF-TDDFT calculations (choice of exchange-correlation functional, basis set, etc.) were the same as reported in Section 2.2 in the main body of our paper. (We did not attempt to 'optimise' these parameters in such a way as to improve agreement with the XMS-CASPT2 method.) The geometries of the E_α and the C isomers were described with a common system of internal coordinates: bond lengths, bond angles and linear combinations of multiple bond angles, torsion angles and linear combinations of multiple torsion angles. Afterwards, the reaction path connecting these two isomers was generated by linear interpolation between them in terms of internal coordinates (LIIC).

An analogous procedure was used to construct reaction paths between the E_α and the Z_α isomers, and between the E_β and the Z_β isomers, except that the choice of internal coordinates was partially different. The choice of internal coordinates for photocyclisation and the the two double-bond photoisomerisations had to be partially different, because the description of the $E_\alpha \rightarrow C$ reaction path requires the inclusion of the C1–C6 distance, which is, however, undesirable for the description of the double-bond photoisomerisations.

The resulting interpolated reaction paths are illustrated in Figure S2. It can be seen that the LIIC procedure leads to physically reasonable reaction paths: the $E_\alpha \rightarrow C$ reaction path involves ring closing, while the $E_\alpha \rightarrow Z_\alpha$ and the $E_\beta \rightarrow Z_\beta$ reaction paths mainly involve intramolecular rotation around the C3=C4 bond.

The benchmark calculations consisted of scanning the energies of the ground state and the low-lying excited states of compound **2** along the interpolated reaction paths at the SF-TDDFT level of theory, and at the XMS-CASPT2 level. These XMS-CASPT2 calculations were performed with the program BAGEL,[10,11] version 1.1.2. The active space of the reference CASSCF calculation included eight electrons distributed in eight π- and π^*-type orbitals, which are shown in Figure S3. The same choice of active space was used for both reaction paths. Along the reaction path for photocyclisation, one π-type orbital

Figure S2: Interpolated reaction paths for (a) photocyclisation ($E_\alpha \rightarrow C$), (b) $E_\alpha \rightarrow Z_\alpha$ photoisomerisation, and (c) $E_\beta \rightarrow Z_\beta$ photoisomerisation. Either reaction path consists of 21 geometries numbered 0 to 20, where the 0-th geometry is the E_α isomer, and the 20-th geometry is the photoproduct. For the sake of clarity, this graphic only shows every other geometry along each reaction path (i.e., geometries 0, 2, 4, ..., 20).

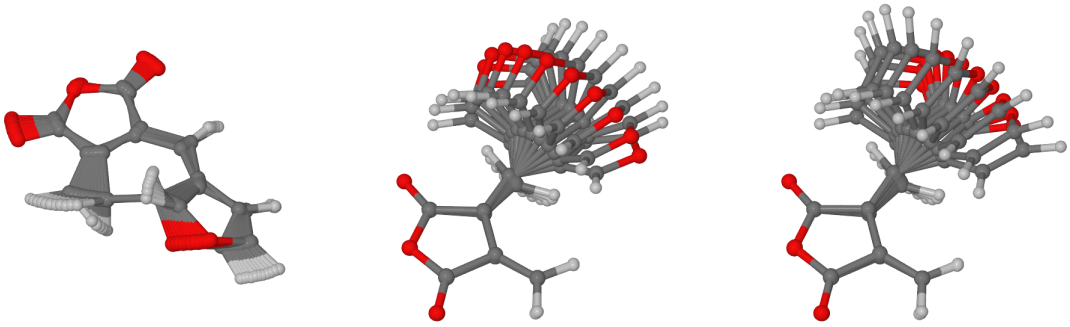

(a) $E_\alpha \rightarrow C$ (b) $E_\alpha \rightarrow Z_\alpha$ (c) $E_\beta \rightarrow Z_\beta$

gradually transforms into the σ-type orbital of the C1–C6 bond, and one π^*-type orbital becomes the corresponding σ^*-type orbital. The lowest three singlet states (i.e. S_0 to S_2) were included in the state-averaging scheme. At the stage of the XMS-CASPT2 calculation, a level shift of 0.2 E_h (hartree) was imposed. We applied the cc-pVDZ basis set[12] in combination with the default density fitting basis set from the BAGEL basis set library, and the so-called single-state single-reference (SS-SR) contraction scheme.[13] We note here that the XMS-CASPT2 calculations do not include the lowest triplet state (T_1), which is, however, necessarily included in the SF-TDDFT calculations.

We discuss first the results of the PES scan along the photocyclisation path ($E_\alpha \rightarrow C$), which are plotted in Figure S4. Panel (a) shows the potential energy curves obtained at the XMS-CASPT2 level. As the molecule begins to move along the reaction path from the E_α structure (leftmost) to the C structure (rightmost), the energy of the S_0 state increases rapidly, while the energies of S_1 and the S_2 excited states slowly decrease. Nearly halfway along the reaction path, the potential energy curves S_1 and the S_2 states exhibit an avoided crossing. Presumably, there exists a conical intersection seam between these states in that region of the configuration space. The existence of the avoided crossing between the S_1 and the S_2 states suggests that the photocyclisation of furylfulgides may, in fact, be best described as a three-state process, a possibility that was not taken into account in previous theoretical studies. In principle, it would have been possible to explore that possibility by including the S_2 state in our NAMD simulations. Unfortunately, however, the inclusion of another electronic state would render the NAMD simulations prohibitively expensive in terms of CPU time, and we were unable to pursue that line of investigation.

As a sidenote, the inspection of the leading configurations of the reference CASSCF wavefunctions shows that both the S_1 and the S_2 states have a substantial contribution from the doubly excited $(\mathrm{MO49})^0\,(\mathrm{MO50})^2$ configuration. Doubly excited states of this type cannot be described with low-level single-reference methods, such as the conventional variant of TDDFT. SF-TDDFT is, however, capable of describing some classes of doubly excited states,[14] and the fact that the S_1 and the S_2 states both have a partial doubly excited character is not a reason to dismiss that method.

A little further along the $E_\alpha \rightarrow C$ reaction path, there is an avoided crossing between the S_1 and the S_0 states. Once the system has passed the avoided crossing, the energy of the S_0 state begins to drop rapidly as the molecule approaches the closed-ring structure (C). On the other hand, the energy of the S_1 state first rises, and then decreases gently.

Panel (b) of Figure S4 shows the potential energy curves calculated at the SF-TDDFT level. A well-known deficiency of SF-TDDFT is that the electronic states obtained with that method suffer from varying degrees of spin contamination: an unphysical mixing between states of different multiplicities. In this case, the expectation value of the total-spin-squared operator ($\hat{S}^2$) for each affected state deviates from the exact value of $S(S+1)$, where S is the total spin quantum number of the given state. For this reason, in addition to the state energies, we plot the expectation values of $\hat{S}^2$. It can be seen that along the entire reaction path, the S_0 and the T_1 states exhibit only slight spin contamination. For the S_1 and the S_2 states, the situation is more complex. At the starting geometry (i.e. the geometry of the E_α isomer), both these states show moderately high spin contamination. As the system evolves along the reaction path, the spin contamination of the S_1 state decreases and becomes negligible from around halfway along the reaction path. On the other hand, the S_2 state is heavily spin-contaminated along the initial and final segments of the reaction path, but around halfway along the reaction path, there is a short segment where the spin contamination is relatively low.

Despite the fact that, at the SF-TDDFT level, the S_1 and especially the S_2 states exhibit spin contamination over a range of molecular geometries, the calculated potential

energy curves are in good agreement with the benchmark provided by the XMS-CASPT2 method. In order to make this point more evident, in Figure S4 (c) we compare the potential energy curves of the singlet states calculated with the two methods. The SF-TDDFT potential energy curves, plotted in black, closely follow those obtained at the XMS-CASPT2 level, in grey.

We now move on to the reaction path for $E_\alpha \rightarrow Z_\alpha$ photoisomerisation. The results of the XMS-CASPT2 calculation are shown in Figure S5 (a). The initial segment of the reaction path from the E_α structure to the Z_α structure corresponds to a sharp rise in the energy of the S_0 state. Meanwhile, the energy of the S_1 state rises slowly, while the energy of the S_2 state decreases. Early along the reaction path, the S_1 and S_2 states exhibit an avoided crossing; past this feature, the energy of the S_1 state begins to decrease, while the energy of the S_2 state rises. Roughly halfway along the reaction path, there is an avoided crossing between the S_1 and the S_0 states. Once the system has passed the avoided crossing, the energy of the S_0 state drops sharply, while the energy of the S_1 state rises gently.

The results of the SF-TDDFT calculation, in turn, are shown in panel (b) of Figure S5. It is immediately apparent that the S_2 state is heavily spin-contaminated along most of the reaction path. What is more, at one of the scan points, a near-degeneracy occurs between the S_0 and the T_1 states, and both become severely spin-contaminated. This is seen as a sudden sharp peak in the $\langle S^2 \rangle$ curve of the S_0 state, and a concurrent sharp dip in the $\langle S^2 \rangle$ curve of the T_1 state. Fortunately, this effect is localised, and does not come into play elsewhere along the reaction path. At other molecular geometries along the interpolated reaction path, the spin contamination of the S_0 and S_1 states is not too severe.

In terms of state energies, SF-TDDFT achieves excellent agreement with XMS-CASPT2 along the entire reaction path for $E_\alpha \rightarrow Z_\alpha$ photoisomerisation. This point is readily apparent in Figure S5 (c), which overlays the potential energy curves for the singlet states calculated with the two methods.

Lastly, Figure S6 shows the results of the PES scans along the reaction path for $E_\beta \rightarrow Z_\beta$ photoisomerisation. The situation is similar as for $E_\alpha \rightarrow Z_\alpha$ photoisomerisation: for the S_0 and S_1 states, SF-TDDFT is in good agreement with XMS-CASPT2, but the S_2 state is heavily spin-contaminated along much of the reaction path.

In summary, the SF-TDDFT method achieves satisfactory agreement with the XMS-CASPT2 benchmark for the PESs of the S_0 and the S_1 states, despite significant spin contamination at some molecular geometries. The S_2 state, on the other hand, is more strongly affected by spin contamination, which means that the SF-TDDFT description of that state is not necessarily reliable enough for it to be included in the NAMD simulations.

The pervasive spin contamination notwithstanding, the close agreement between XMS-CASPT2 and SF-TDDFT for PESs is very encouraging, and bodes well for the applicability of the latter method in simulations of large photoactive molecules. As regards spin contamination, recent work by Filatov, Choi and coworkers[15–17] has demonstrated that this artefact can be eliminated, further improving the performance of SF-TDDFT. These authors have developed a mixed-reference variant of SF-TDDFT (MR-SF-TDDFT) which employs a combination of the $M_S = +1$ and $M_S = -1$ (or, $|\alpha\alpha\rangle$ and $|\beta\beta\rangle$) components of the DFT triplet state as the reference state.[15–17] In this approach, spin contamination is largely removed.[15] Owing to the absence of spin contamination, MR-SF-TDDFT is expected to be generally superior in terms of accuracy to conventional SF-TDDFT.

Figure S3: CASSCF active space natural orbitals of compound **2**, plotted in the form of isosurfaces with isovalues of $\pm 0.05\ {a_0}^{-3/2}$. The orbitals were generated through a SA-3-CASSCF(8,8)/cc-pVDZ calculation at the SF-TDDFT-optimised ground-state equilibrium geometry of the E_α isomer. The qualitative chemical character of each orbital is given in brackets.

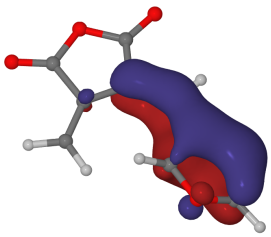

(a) MO46 (π)

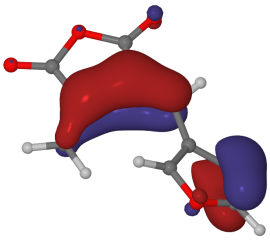

(b) MO47 (π)

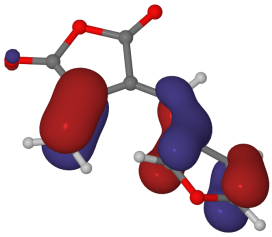

(c) MO48 (π)

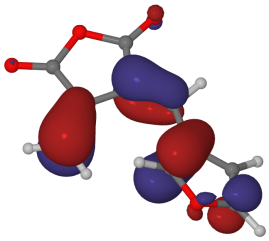

(d) MO49 (π)

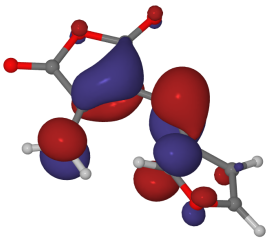

(e) MO50 (π^*)

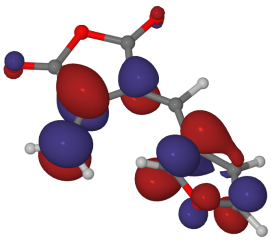

(f) MO51 (π^*)

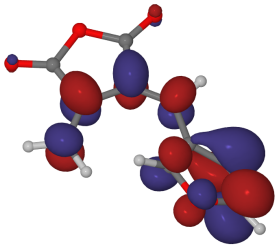

(g) MO52 (π^*)

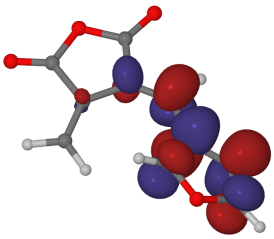

(h) MO53 (π^*)

Figure S4: Energies of the lowest few electronic states of model furylfulgide **2** along a reaction path leading from the E_α isomer to the C isomer, calculated with the (a) XMS-CASPT2 and (b) SF-TDDFT methods. For the latter method, panel (b) also shows values of $\langle S^2 \rangle$ for each state. Panel (c) compares the potential energy curves of the singlet states obtained with the two methods.

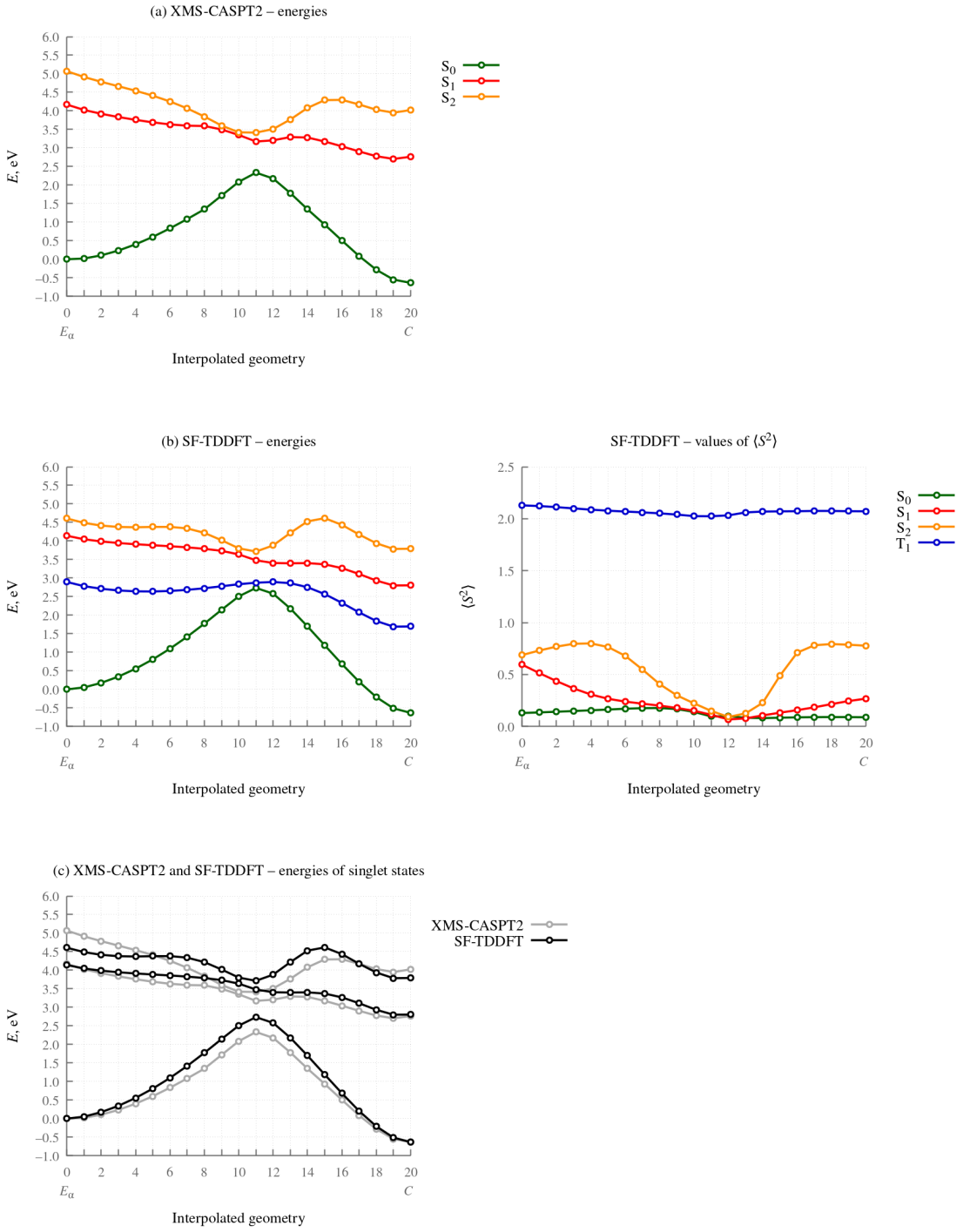

Figure S5: Energies of the lowest few electronic states of model furylfulgide **2** along a reaction path leading from the E_α isomer to the Z_α isomer, calculated with the (a) XMS-CASPT2 and (b) SF-TDDFT methods. For the latter method, panel (b) also shows values of $\langle S^2 \rangle$ for each state. Panel (c) compares the potential energy curves of the singlet states obtained with the two methods.

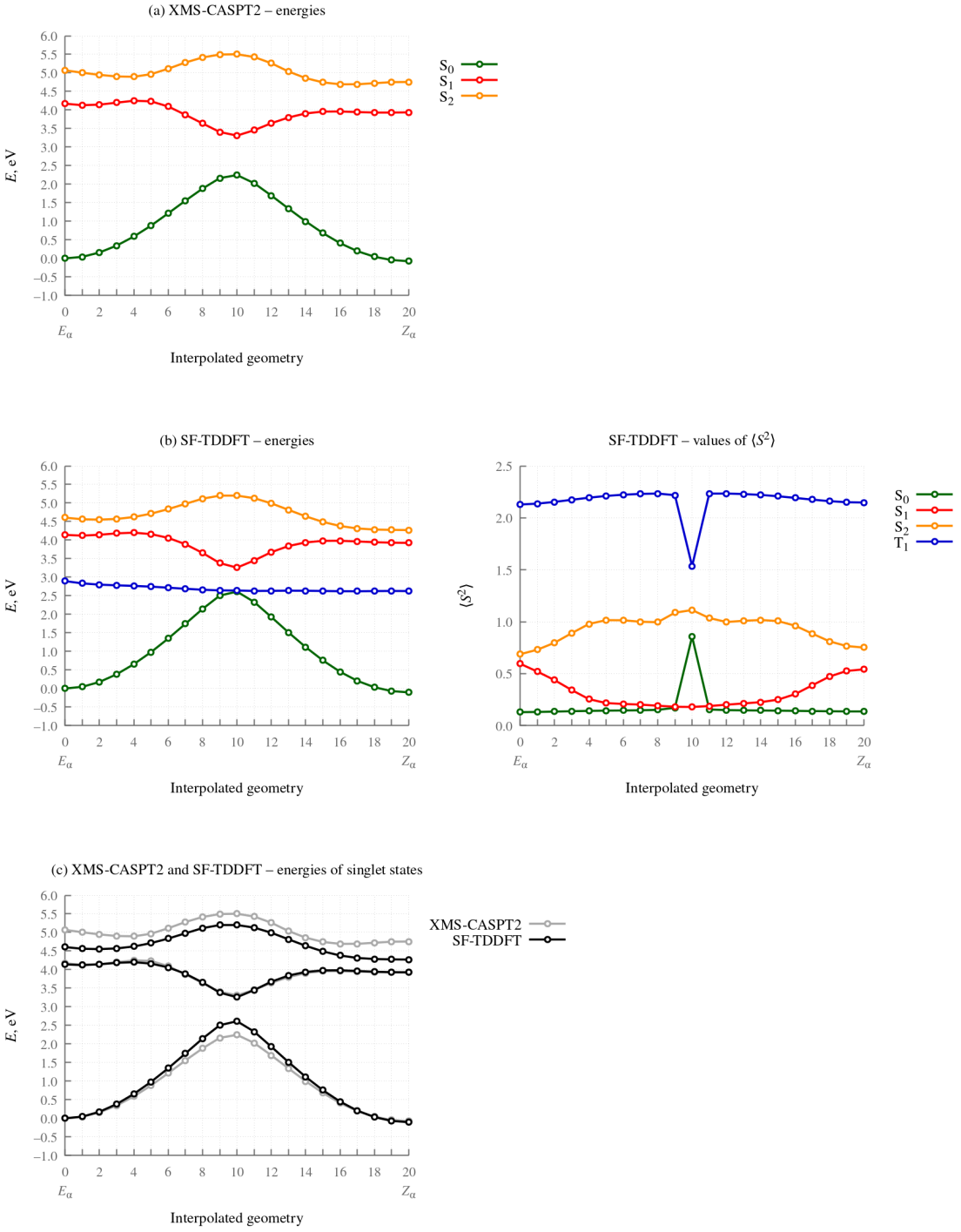

Figure S6: Energies of the lowest few electronic states of model furylfulgide **2** along a reaction path leading from the E_β isomer to the Z_β isomer, calculated with the (a) XMS-CASPT2 and (b) SF-TDDFT methods. For the latter method, panel (b) also shows values of $\langle S^2 \rangle$ for each state. Panel (c) compares the potential energy curves of the singlet states obtained with the two methods.

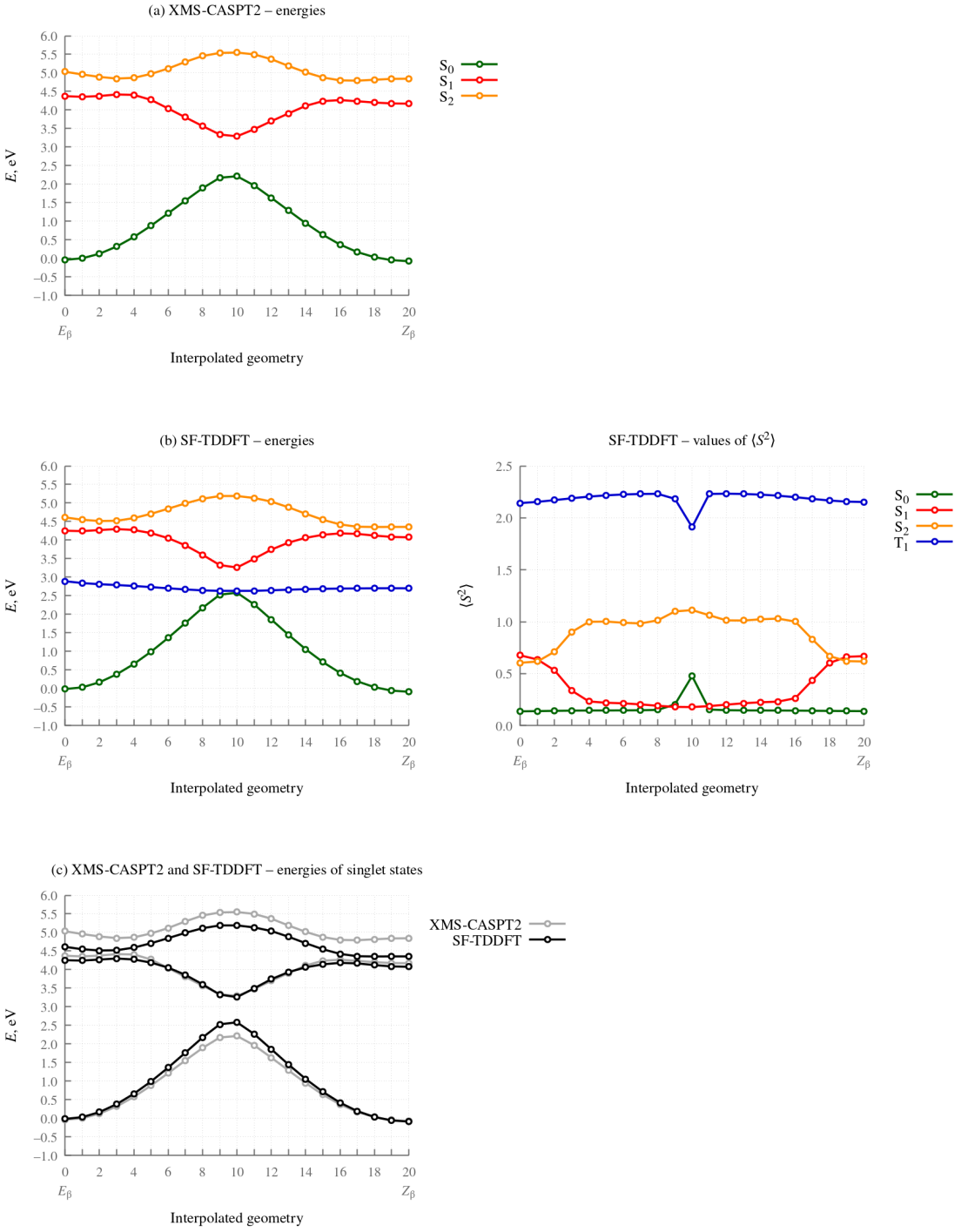

S2 PES Scan Along the Torsional Degrees of Freedom

As noted in the main body of our paper, in the S_1 state the E_α isomer of furylfulgide Me-**1** is quite flexible, and can undergo cyclisation as well as rotation around the C3=C4 bond ($E \rightarrow Z$ photoisomerisation). The latter process may potentially be accompanied by a rotation around the adjacent C2–C3 bond. In order to shed more light on the interplay between these two intramolecular rotations, we mapped out the topography of the PES of the S_1 state as a function of the torsion angles C1=C2–C3=C4 (τ_{1234}) and C2–C3=C4–C5 (τ_{2345}). For the sake of computational efficiency, this two-dimensional PES scan was performed for the truncated model compound **2**, and then only with the use of the SF-TDDFT method. The atom numbering and the relevant torsion angles are shown schematically in Figure S7 (a) on the following page.

In the course of the scan, τ_{1234} was constrained at values ranging from 0° to 360° in steps of 10°, while τ_{2345} was constrained at values from 0° to 180° in steps of 10°. (Note that $\tau_{1234} = 0°$ is equivalent to $\tau_{1234} = 360°$.) All other degrees of freedom were re-optimised at each scan point (it was effectively a relaxed PES scan). On the technical side, the PES scan was performed by interfacing Q-Chem to Gaussian 16, Revision A.03.[18] In this setup, Gaussian acts as a "wrapper" around Q-Chem, and carries out the geometry optimisation by calling Q-Chem for the calculation of the energy and gradient. As per the default settings in Gaussian 16, the geometries were optimised with the use of the Berny algorithm in redundant internal coordinates.[19–26]

The topography of the PES of the S_1 state is presented in Figure S7 (b). There is a deep potential energy well in in the region $\tau_{1234} \approx 0°$ and $\tau_{2345} \approx 0°$, which is labelled W-I. The reason this well exists is because, for near-zero values of the two torsion angles, the geometry optimisations of the S_1 state collapse towards the closed-ring isomer. A second potential energy well (W-II) is located at $\tau_{1234} \approx 0°$ and $\tau_{2345} \approx 90°$, and a third (W-III) at $\tau_{1234} \approx 180°$ and $\tau_{2345} \approx 90°$. The wells W-II and W-III correspond to a roughly 90° rotation around the C3=C4 bond. In the region near the minimum of each of the three potential energy wells, the S_1 state is near-degenerate with the S_0 state.

Let us now consider what will happen to a molecule of the E_α isomer following photoexcitation into the S_1 state. One possibility is that the molecule will undergo cyclisation. In terms of the topography of the PES of the S_1 state along the two torsion angles, this means relaxation towards the bottom of the well W-I. Another possible relaxation pathway is rotation around the C3=C4 bond. This process leads towards the bottom of the well W-II. In Figure S7 (b), it is indicated with a red arrow. It can be seen that rotation around the C3=C4 bond is favoured by the downward slope of the PES of the S_1 state in the positive τ_{2345} direction. Conversely, there appears to be no driving force for rotation around the C2–C3 bond, regardless of whether it is accompanied by a rotation around the C3=C4 bond.

Regarding, in turn, the E_β isomer, following photoexcitation into the S_1 state it will begin to undergo a rotation around the C3=C4 bond, relaxing downwards towards the well W-III. In Figure S7 (b), this pathway is indicated with a yellow arrow. As with the E_α isomer, for the E_β isomer there seems to be no driving force for a rotation around the C2–C3 bond. The PES scan also confirms that the E_β isomer is incapable of photocyclisation, as is not feasible for it to reach the well W-I.

A connection can be drawn to the NAMD simulations of the excited-state relaxation dynamics of furylfulgide Me-**1**. Unlike model compound **2**, furylfulgide Me-**1** has methyl substituents on atoms C1 and C6. (All practically relevant furylfulgides have alkyl substituents at these positions in order to prevent the elimination of dihydrogen from the closed-ring form.) For steric reasons, these methyl groups are expected to hinder rotation around the C2–C3 bond when the torsion angle τ_{2345} is close to zero. This, and the general

Figure S7: (a) Atom numbering and schematic illustration of the PES scan along the torsion angles τ_{1234} and τ_{2345} of furylfulgide **2**. In this graphic, the molecule is in the E_α isomeric form.

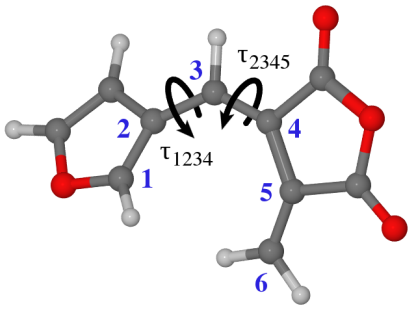

(b) Energy of the S_1 state as a function of τ_{1234} and τ_{2345}. The zero of the energy scale corresponds to the energy of the ground-state equilibrium geometry of the E_α isomer. The labels E_α and E_β indicate the approximate locations of the two E-type isomers. The three main potential energy wells are labelled W-I, W-II, and W-III. (W-I and W-III straddle the $\tau_{1234} = 360°$ line.)

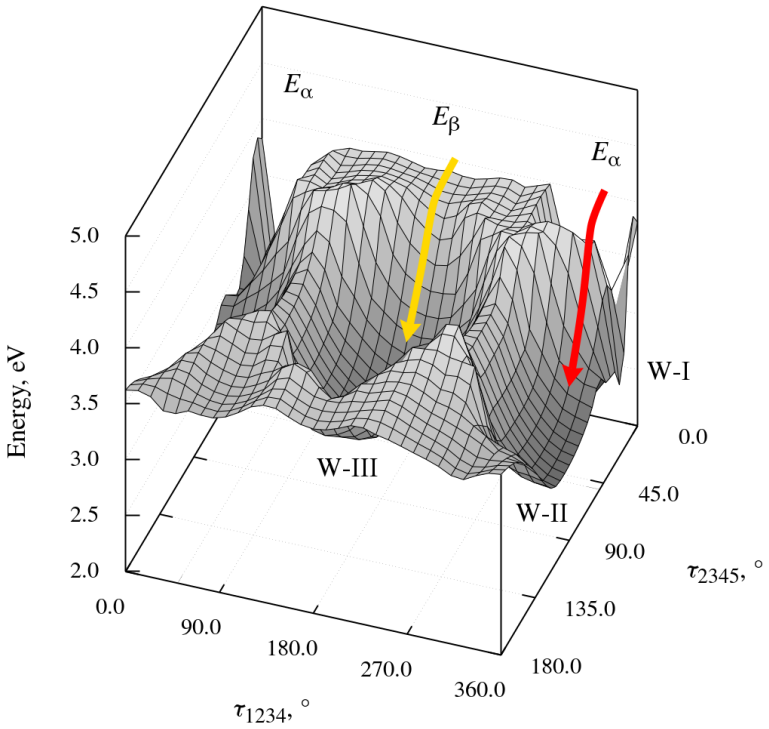

---

lack of driving force for rotation around the C2–C3 bond in the S_1 state, is presumably the reason that the E_α and E_β isomers do not interconvert while the molecule is in the S_1 state. The lack of interconversion between the E_α and the E_β isomers in the S_1 state is an example of the non-equilibration of excited rotamers (NEER) effect,[27,28] in which the photochemical reaction of each rotamer occurs faster than interconversion between the

various rotamers in the excited state.

Given the fact that rotation around the C2–C3 bond does not appear to be driven by the topography of the PES of the S_1 state, we hypothesize that when a partial rotation does occur in our simulations, it is caused by a redistribution of energy from other vibrational modes. In particular, internal conversion from the S_1 state into the S_0 state and subsequent relaxation in the S_0 state releases a large amount of energy into the vibrational modes of the molecule. Presumably, a fraction of that energy is transferred into the mode which corresponds to rotation around the C2–C3 bond.

S3 $E_\alpha \rightleftharpoons E_\beta$ Equilibrium

In the present section, we estimate the relative abundances of the E_α and E_β isomers of furylfulgide Me-**1** at thermal equilibrium. (For reference, the structures of the two isomers are shown in Figure S8 below.) This information will later be used in Section 3.3.1 in the main body of our paper in order to predict the photoproduct distribution of Me-**1** in the solution phase. The equilibrium populations of the two isomers were estimated by optimizing their respective ground-state geometries, and calculating their relative free energies.

The geometry optimisations were carried out at the density functional theory (DFT) level. In order to gain a measure of how sensitive the calculated free energy difference is to the choice of exchange-correlation functional, the optimisations were performed with several functionals: the pure generalised gradient approximation (GGA) functional B97-D3,[29] the global hybrid GGA functional B3LYP,[30,31] the meta-GGA functional TPSS[32] and the global hybrid meta-GGA functionals PW6B95[33] and M06-2X.[34] Another reason for us to use multiple functionals is that the energy difference between the E_α and E_β isomers is relatively small, on the order of a few kJ/mol. As such, it is comparable to the accuracy of DFT for relative energies. We believe that no one functional can be singled out as providing the best estimate of the free energy difference (ΔG) between the two isomers. Rather, it seems more appropriate to interpret the spread in the calculated ΔG values as a confidence interval for our estimate of the free energy difference.

For the first four functionals in the above list, the calculated energies and gradients were corrected for dispersion effects via the 'D3' semiempirical correction scheme of Grimme and coworkers with Becke-Johnson damping.[35] When discussion the simulation results, the

Figure S8: Thermal equilibrium between the E_α and E_β isomers of furylfulgides in the series **1**.

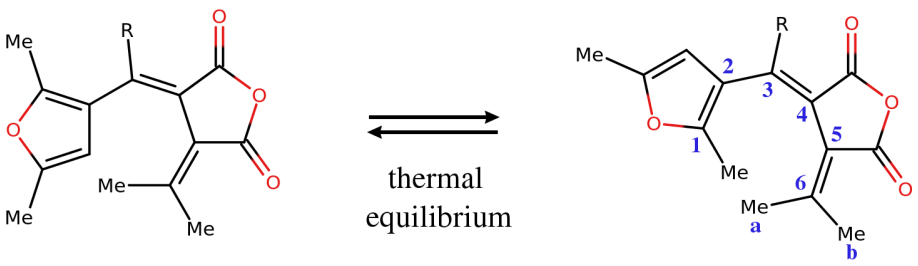

1-E_β **1**-E_α

inclusion of the dispersion correction is noted by adding the suffix -D3(BJ). All DFT calculations were performed in the program Gaussian 16, Revision A.03.[18] The def2-TZVP basis set[36] was used. When performing calculations with the functionals B97-D3 and B3LYP, we used the default ultrafine integration grid. In the case of the functionals TPSS, PW6B95, and M06-2X, we imposed the more accurate superfine grid. The free energy calculations were performed for a temperature of 298 K. All calculations were performed *in vacuo*, which is to say, for an isolated molecule. The neglect of solvent effects is justified by the fact that the experimental measurements of the product distribution of furylfulgide Me-**1** were performed in toluene,[37] a nonpolar solvent which is unlikely to have a significant influence on the $E_\alpha \rightleftharpoons E_\beta$ equilibrium.

As a verification of the predictions of DFT, we re-calculated the single-point energies of the E_α and E_β isomers of Me-**1** with the use of the domain-based local pair natural orbital (DLPNO) variant[38,39] of the coupled cluster with perturbative triples (CCSD(T)) method.[40] The DLPNO-CCSD(T) calculations were performed at molecular geometries optimised with the B3LYP-D3(BJ) method. In the subsequent calculation of free energy difference, the zero-point vibrational energies and the thermal corrections were likewise taken from the B3LYP-D3(BJ) calculation. We denote this composite level of theory as DLPNO-CCSD(T)//B3LYP-D3(BJ).

The DLPNO-CCSD(T) calculations were performed with the program Orca, version 4.2.1.[41,42] As regards the choice of basis set in these calculations, the inclusion of diffuse basis functions is necessary in order for the calculation to capture intramolecular dispersion interactions, such as between the furyl group and the dimethylmethylene (=CMe_2) group. For this reason, we used the jun-cc-pVTZ basis set, which is one of the so-called calendar basis sets introduced by Papajak et al.[43] These basis sets are derived through the successive elimination of diffuse basis functions from the standard aug-cc-pVnZ basis sets, starting with the diffuse subshells with the highest angular momentum. In particular, the jun-cc-pVTZ basis set is obtained from aug-cc-pVTZ by removing the diffuse f functions second-row elements, as well as all diffuse functions from hydrogen. Thus, only the s, p, and d diffuse functions on the second-row elements are retained. Moreover, in the DLPNO-CCSD(T) calculations we imposed the resolution-of-the-identity (RI) approximation for the calculation of both Coulomb integrals and exchange integrals. We employed the standard aug-cc-pVTZ/C and aug-cc-pVTZ/JK auxiliary basis sets from the Orca basis set library. A restricted Hartree-Fock (RHF) reference determinant was used.

The results of the various calculations are summarised in Table S1 on the following page. All five functionals that we have taken into consideration agree in predicting that the E_β isomer of Me-**1** has a slightly higher free energy than the E_α isomer. The calculated ΔG values fall in the range from 2.4 kJ/mol (the value obtained in the B97-D3(BJ) calculation) to 5.0 kJ/mol (the value from the PW6B95-D3(BJ) calculation). The DLPNO-CCSD(T)//B3LYP-D3(BJ) composite calculation gives a value of 3.2 kJ/mol, which is within the range of the values obtained in the pure DFT calculations. As noted before, there is no compelling reason to favour any one of the calculated ΔG values over another; rather, we take the spread in the calculated ΔG values as an indication of the systematic uncertainty in the true free energy difference. It seems reasonable to infer that the true ΔG value lies within the range of the theoretically-predicted ΔG values. Hence, our final estimate of the free energy difference is $\Delta G = 3.5 \pm 1.5$ kJ/mol. On the basis of this value, the mole fraction of the E_α isomer is estimated as $x(E_\alpha) = 0.8 \pm 0.1$, and that of the E_β isomer as $x(E_\beta) = 0.2 \pm 0.1$.

Table S1: Calculated free energy difference $\Delta G = G(E_\beta) - G(E_\alpha)$ for the $E_\alpha \rightleftharpoons E_\beta$ isomerisation of furylfulguide Me-**1**. $x(E_\alpha)$ is the mole fraction of the E_α isomer at equilibrium.

Level of theory	ΔG, kJ/mol	$x(E_\alpha)$
B97-D3(BJ)	2.4	0.72
B3LYP-D3(BJ)	2.8	0.76
TPSS-D3(BJ)	2.5	0.74
PW6B95-D3(BJ)	5.0	0.88
M06-2X	4.6	0.87
DLPNO-CCSD(T) [a]	3.2	0.79

[a] DLPNO-CCSD(T)//B3LYP-D3(BJ) composite calculation.

S4 Uncertainty Analysis

This section expands on the discussion of uncertainty in calculated quantum yields which was begun in Section 2.4 in the main body of the present paper. As mentioned there, for a given photoproduct P, the quantum yields of the $E_\alpha \rightarrow P$ and $E_\beta \rightarrow P$ processes are estimated as:

$$\Phi(E_\alpha \rightarrow P) = \frac{N(E_\alpha \rightarrow P)}{N_{\text{trajs}}(E_\alpha)} \tag{1a}$$

and

$$\Phi(E_\beta \rightarrow P) = \frac{N(E_\beta \rightarrow P)}{N_{\text{trajs}}(E_\beta)} \tag{1b}$$

Here, $N_{\text{trajs}}(E_\alpha)$ is the total number of trajectories which were propagated for the E_α isomer, and $N(E_\alpha \rightarrow P)$ is number of snapshots assigned to the cluster associated with photoproduct P among these trajectories at $t = 500$ fs. The notation for the $E_\beta \rightarrow P$ process is analogous.

Moreover, the overall quantum yield of photoproduct P in a sample containing an equilibrium mixture of the E_α and E_β isomers is estimated as:

$$\Phi_{\text{OA}}(P) = x(E_\alpha)\,\Phi(E_\alpha \rightarrow P) + x(E_\beta)\,\Phi(E_\beta \rightarrow P) \tag{2}$$

where $x(E_\alpha)$ and $x(E_\beta)$ are, respectively, the mole fractions of the E_α and E_β isomers.

Until now, we have not taken into account the fact that the quantum yields are calculated on the basis of a finite number of simulated trajectories and, as such, they are subject to statistical uncertainties. In the case of a single isomer (either E_α or E_β), a set of simulated trajectories can be considered as binomial experiment: a series of success-failure experiments (or, Bernoulli trials) in which success corresponds the formation of photoproduct P, and failure corresponds to any other outcome. The estimated quantum yield of photoproduct P is then equivalent to the observed binomial proportion – the number of successes divided by the number of experiments.

The results of a binomial experiment are conventionally expressed in terms of a confidence interval (CI) for the probability of success. There are several methods for calculating this CI,

with various accuracy and computational complexity. For the sake of simplicity, in the present study we used the normal approximation interval[44] (Wald interval). This approach gives the following expressions for the CIs for the quantum yields of the $E_\alpha \rightarrow P$ and $E_\beta \rightarrow P$ processes:

$$\text{CI for } \Phi(E_\alpha \rightarrow P): \quad \hat{p}_1 \pm z \sqrt{\frac{\hat{p}_1\,(1-\hat{p}_1)}{N_{\text{trajs}}(E_\alpha)}} \tag{3a}$$

and

$$\text{CI for } \Phi(E_\beta \rightarrow P): \quad \hat{p}_2 \pm z \sqrt{\frac{\hat{p}_2\,(1-\hat{p}_2)}{N_{\text{trajs}}(E_\beta)}} \tag{3b}$$

Here, $\hat{p}_1 = N(E_\alpha \rightarrow P)\,/\,N_{\text{trajs}}(E_\alpha)$ is the observed binomial proportion for the $E_\alpha \rightarrow P$ process, and $\hat{p}_2 = N(E_\beta \rightarrow P)\,/\,N_{\text{trajs}}(E_\beta)$ is the same quantity for the $E_\beta \rightarrow P$ process. z is the $(1-\alpha/2)$-th quantile of the normal distribution corresponding to the target error rate α. For a 95% confidence level, $\alpha = 0.05$ and $z = 1.96$.

We now move on to the more complex case of sample containing both the E_α and the E_β isomers in thermal equilibrium. The overall quantum yield calculated via equation 2 is equivalent to a weighted sum of two binomial proportions, with the added complication that the weights (the mole fractions of the two isomers) are subject to systematic uncertainty. We address the statistical uncertainty first. The expression for the Wald interval for the weighted sum of two binomial proportions was given by Decrouez and Robison:[45]

$$\text{CI for } \Phi_{\text{OA}}(P): \quad \hat{p}_{\text{OA}} \pm \underbrace{z \sqrt{[x(E_\alpha)]^2\ \frac{\hat{p}_1\,(1-\hat{p}_1)}{N_{\text{trajs}}(E_\alpha)} + [x(E_\beta)]^2\ \frac{\hat{p}_2\,(1-\hat{p}_2)}{N_{\text{trajs}}(E_\beta)}}}_{\Delta\Phi_{\text{OA}}^{\text{stat}}} \tag{4}$$

where $\hat{p}_{\text{OA}} = x(E_\alpha)\,\hat{p}_1 + x(E_\beta)\,\hat{p}_2$. The term labelled $\Delta\Phi_{\text{OA}}^{\text{stat}}$ is the statistical contribution to the uncertainty in the overall quantum yield.

Having taken into account the statistical contribution to the uncertainty, we now turn our attention to the systematic contribution. The latter arises from the fact that the calculation of the overall quantum yield requires the knowledge of the population ratio of the E_α and the E_β isomers, which is, however, not known exactly. The systematic uncertainty in the population ratio will propagate into a systematic uncertainty in the overall quantum yield. In order to follow the propagation of uncertainty, let us note that the mole fractions of the two isomers are subject to the constraint $x(E_\alpha) + x(E_\beta) = 1$. This is because only the E_α and the E_β isomers are present prior to the irradiation of the sample. Taking advantage of that constraint, the expression for the estimated overall quantum yield (equation 2) can be rewritten in a form that contains the mole fraction of only a single isomer:

$$\Phi_{\text{OA}}(P) = x(E_\alpha)\,\hat{p}_1 + [1 - x(E_\alpha)]\ \hat{p}_2 \tag{5}$$

Here, we have chosen $x(E_\alpha)$ as the independent variable.

For a function $f = f(x)$ of a single variable x whose value lies in the range of $x_0 \pm \Delta x$, the bound Δf for the systematic uncertainty is given by:[46]

$$\Delta f = \left| \frac{\mathrm{d}f}{\mathrm{d}x}(x_0)\,\Delta x \right| \tag{6}$$

The systematic contribution to the uncertainty in $\Phi_{\mathrm{OA}}(P)$ is therefore:

$$\Delta\Phi_{\mathrm{OA}}^{\mathrm{syst}} = \left| \frac{\mathrm{d}\Phi_{\mathrm{OA}}(P)}{\mathrm{d}x(E_\alpha)}\,\Delta x(E_\alpha) \right| = \left| \,(\hat{p}_1 - \hat{p}_2)\,\Delta x(E_\alpha)\,\right| \tag{7}$$

The minus sign in the term $(\hat{p}_1 - \hat{p}_2)$ reflects the fact that the more the photoproduct distributions of the E_α and the E_β isomers differ from one another, the larger the uncertainty in the overall quantum yields.

Finally, the statistical and systematic uncertainties are combined into a final 'joint' CI for the overall quantum yield:

$$\text{joint CI for } \Phi_{\mathrm{OA}}(P): \quad \hat{p}_{\mathrm{OA}} \pm \sqrt{\left(\Delta\Phi_{\mathrm{OA}}^{\mathrm{stat}}\right)^2 + \left(\Delta\Phi_{\mathrm{OA}}^{\mathrm{syst}}\right)^2} \tag{8}$$

Equation 8 is our working equation for estimating the confidence interval in $\Phi_{\mathrm{OA}}(P)$.

S5 Molecular Geometries

In order to ensure that our results can be reproduced by other researchers, the present section lists selected molecular geometries of furylfulgides Me-**1** and **2**. All geometries are given in terms of Cartesian coordinates in units of ångström (Å). The level of electronic structure theory at which the given structure was optimised is given in the relevant entry.

Furylfulgide Me-1

Ground-state equilibrium geometry of the E_α isomer of furylfulgide Me-**1**, optimised at the DFT (50-50/6-31G(d)) level of theory. The simulation parameters are given in Section 2.2 in the main body of our paper.

C	-2.553456	5.619255	12.878165
C	-3.963306	5.941924	12.602265
C	-2.516136	5.318885	14.331006
C	-4.711250	5.396846	13.759498
C	-1.499797	5.406604	12.059377
C	-4.515479	6.779918	11.705962
C	-1.616225	5.308413	10.604276
C	-0.714683	5.873504	9.635315
C	-2.499685	4.562281	9.890542
C	-1.133891	5.461525	8.426162
C	-3.622690	3.670408	10.252577
C	-0.666330	5.702399	7.043109
C	-0.102334	5.192785	12.567415
C	-3.703012	7.571807	10.733442
C	-5.988184	7.039976	11.618597
O	-3.805279	5.124503	14.748388
O	-1.616743	5.195720	15.098866
O	-5.871238	5.212081	13.943379
O	-2.214766	4.657620	8.574259
H	0.118125	6.521626	9.829000
H	-0.408075	4.768938	6.548111
H	0.212589	6.337749	7.054982
H	-1.433423	6.189479	6.444933
H	0.297946	4.263340	12.168835
H	0.537151	5.991556	12.193416
H	-0.045396	5.182720	13.644619
H	-6.313923	6.893227	10.589035
H	-6.190460	8.083717	11.857509
H	-6.573944	6.408444	12.268204
H	-4.153438	8.552696	10.599946
H	-3.686006	7.090008	9.756662
H	-2.676130	7.695803	11.053134
H	-3.607607	2.779806	9.630924
H	-4.586518	4.158368	10.115521
H	-3.549313	3.373226	11.292180

Ground-state equilibrium geometry of the E_β isomer of furylfulgide Me-**1**, optimised at the DFT (50-50/6-31G(d)) level of theory. The simulation parameters are given in Section 2.2 in the main body of our paper.

C	-2.992150	5.212328	12.787381
C	-3.825689	6.413934	12.650826
C	-3.326427	4.666489	14.117186
C	-4.878110	6.263071	13.684700
C	-2.240332	4.516270	11.905976
C	-3.593326	7.571257	12.004712
C	-2.246825	4.812509	10.472501
C	-3.402868	5.119333	9.671461
C	-1.202306	4.771238	9.603020
C	-2.979053	5.229938	8.400863
C	0.258351	4.568678	9.746772
C	-3.659015	5.495784	7.113705
C	-1.449746	3.310382	12.346585
C	-2.331842	7.827573	11.245585
C	-4.542178	8.728788	12.023063
O	-4.474471	5.278147	14.546896
O	-2.809157	3.817293	14.770281
O	-5.898200	6.843943	13.873066
O	-1.637410	5.032539	8.353801
H	-4.413744	5.210445	10.017347
H	-3.260791	6.386982	6.633528
H	-4.720618	5.642094	7.280415
H	-3.531989	4.665749	6.422239
H	-0.674917	3.579536	13.058727
H	-2.087301	2.598051	12.860730
H	-0.998705	2.817133	11.495146
H	-4.769385	9.016567	10.996575
H	-4.061910	9.591281	12.484101
H	-5.464190	8.515933	12.541687
H	-2.019495	8.857495	11.403046
H	-2.490067	7.697109	10.176250
H	-1.528711	7.166448	11.545163
H	0.540569	4.518988	10.791367
H	0.800271	5.391165	9.285920
H	0.582066	3.651047	9.259056

Furylfulgide 2

Ground-state equilibrium geometry of the E_α isomer of model furylfulgide **2**, optimised at the SF-TDDFT (50-50/6-31G(d)) level of theory. The simulation parameters are given in Section 2.2 in the main body of our paper.

C	-2.711413	5.656338	12.797291
C	-4.112539	6.009667	12.666429
C	-2.449874	5.582279	14.256974
C	-4.645597	6.062503	14.052633
C	-1.691226	5.431636	11.961464
C	-4.898448	6.343047	11.640689
C	-1.655536	5.353307	10.519858
C	-0.501123	5.618315	9.704687
C	-2.609281	4.928086	9.650024
C	-0.863902	5.353367	8.439845
O	-3.623123	5.808836	14.923465
O	-1.435784	5.362665	14.830034
O	-5.748864	6.288682	14.421951
O	-2.144634	4.922972	8.399540
H	0.453412	5.973873	10.041339
H	-0.740919	5.276028	12.451354
H	-3.602532	4.552895	9.785803
H	-4.553305	6.367921	10.624184
H	-5.918453	6.626663	11.837422
H	-0.360939	5.414359	7.496881

Ground-state equilibrium geometry of the E_β isomer of model furylfulgide **2**, optimised at the SF-TDDFT (50-50/6-31G(d)) level of theory. The simulation parameters are given in Section 2.2 in the main body of our paper.

C	-2.716420	5.738139	12.797570
C	-4.148798	5.939566	12.687569
C	-2.424647	5.717587	14.251721
C	-4.667086	5.907719	14.080503
C	-1.692914	5.590865	11.946056
C	-4.972944	6.240835	11.682792
C	-1.678894	5.453573	10.511592
C	-2.680314	4.991654	9.587541
C	-0.584339	5.701356	9.744414
C	-2.108290	5.017594	8.373008
O	-3.607843	5.793266	14.936286
O	-1.382121	5.635227	14.810526
O	-5.785563	5.983431	14.465341
O	-0.833520	5.460427	8.458791
H	-3.665740	4.641045	9.817126
H	-0.724183	5.550392	12.422343
H	0.398287	6.056068	9.984227
H	-4.640990	6.357491	10.668227
H	-6.015398	6.405049	11.897256
H	-2.447823	4.756507	7.391884

Ground-state equilibrium geometry of the Z_α isomer of model furylfulgide **2**, optimised at the SF-TDDFT (50-50/6-31G(d)) level of theory. The simulation parameters are given in Section 2.2 in the main body of our paper.

C	-2.532706	5.460328	12.886094
C	-3.838638	6.022963	12.566023
C	-2.500102	5.338013	14.352149
C	-4.530833	6.215831	13.861678
C	-1.565999	5.129447	12.011867
C	-4.421610	6.346462	11.417297
C	-0.250951	4.578931	12.174482
C	0.633431	4.305022	11.070424
C	0.451429	4.205531	13.287671
C	1.758547	3.805267	11.598765
O	-3.689932	5.794615	14.855169
O	-1.651617	4.931907	15.080957
O	-5.610931	6.647331	14.088254
O	1.650371	3.743913	12.948120
H	0.428755	4.470116	10.030023
H	-1.815312	5.310919	10.975874
H	0.208470	4.223082	14.327820
H	-3.938754	6.214296	10.463604
H	-5.416421	6.757804	11.423799
H	2.684273	3.460303	11.187051

Ground-state equilibrium geometry of the Z_β isomer of model furylfulgide **2**, optimised at the SF-TDDFT (50-50/6-31G(d)) level of theory. The simulation parameters are given in Section 2.2 in the main body of our paper.

C	-2.520624	5.512030	12.920183
C	-3.853850	5.981511	12.568327
C	-2.424602	5.648141	14.387416
C	-4.501256	6.377706	13.839684
C	-1.590693	5.054852	12.064361
C	-4.490783	6.091126	11.406336
C	-0.253944	4.565899	12.246578
C	0.593330	4.379206	13.396323
C	0.497902	4.152793	11.185451
C	1.746605	3.883063	12.925742
O	-3.611072	6.155252	14.852523
O	-1.540823	5.399826	15.141445
O	-5.585298	6.815604	14.034437
O	1.696397	3.741725	11.574723
H	0.340586	4.596858	14.412121
H	-1.898587	5.049358	11.027773
H	0.291977	4.106656	10.134081
H	-4.041679	5.810676	10.468421
H	-5.496646	6.474078	11.386118
H	2.665331	3.586990	13.388206

Ground-state equilibrium geometry of the *C* isomer of model furylfulgide **2**, optimised at the SF-TDDFT (50-50/6-31G(d)) level of theory. The simulation parameters are given in Section 2.2 in the main body of our paper.

C	-2.506874	5.523872	12.968716
C	-3.738807	5.811524	12.512051
C	-2.594275	5.421164	14.442689
C	-4.639882	5.910565	13.657853
C	-1.340305	5.434284	12.138513
C	-4.030811	6.077873	11.073151
C	-1.581345	5.429928	10.816721
C	-0.765949	5.545681	9.641117
C	-2.994448	5.301413	10.290470
C	-1.606212	5.715707	8.610628
O	-3.895582	5.650132	14.793321
O	-1.741157	5.191784	15.233218
O	-5.798759	6.160601	13.705742
O	-2.907727	5.686508	8.917630
H	0.304896	5.581546	9.594478
H	-0.354194	5.432926	12.567613
H	-3.256478	4.241035	10.301399
H	-3.940309	7.146222	10.864696
H	-5.037466	5.779889	10.799045
H	-1.388387	5.890756	7.572817

References

[1] Y. Shao, M. Head-Gordon, and A. I. Krylov, *J. Chem. Phys.,* 2003, **118**, 4807–4818.

[2] J. M. Herbert and A. Mandal, *ChemRxiv*, 2022.

[3] T. Shiozaki, W. Győrffy, P. Celani and H. J. Werner, J. Chem. Phys., 2011, **135**, 081106.

[4] P. Pulay, *Int. J. Quantum Chem.*, 2011, **111**, 3273–3279.

[5] H. Lischka, D. Nachtigallová, A. J. A. Aquino, P. G. Szalay, F. Plasser, F. B. C. Machado and M. Barbatti, *Chem. Rev.*, 2018, **118**, 7293–7361.

[6] J. W. Park, R. Al-Saadon, M. K. MacLeod, T. Shiozaki and B. Vlaisavljevich, *Chem. Rev.*, 2020, **120**, 5878–5909.

[7] T. Shiozaki, C. Woywod and H. J. Werner, *Phys. Chem. Chem. Phys.*, 2013, **15**, 262–269.

[8] J. W. Park and T. Shiozaki, *Mol. Phys.*, 2018, **116**, 2583–2590.

[9] S. Sen and I. Schapiro, *Mol. Phys.*, 2018, **116**, 2571–2582.

[10] BAGEL, Brilliantly Advanced General Electronic-structure Library. http://www.nubakery.org under the GNU General Public License.

[11] T. Shiozaki, *WIREs Comput. Mol. Sci.*, 2017, e1331.

[12] T. H. Dunning Jr, *J. Chem. Phys.*, 1989, **90**, 1007–1023.

[13] J. Finley, P. A. Malmqvist, B. O. Roos and L. Serrano-Andrés, *Chem. Phys. Lett.*, 1998, **288**, 299–306.

[14] D. Casanova and A. I. Krylov, *Phys. Chem. Chem. Phys.*, 2020, **22**, 4326–4342.

[15] S. Lee, M. Filatov. S. Lee and C. H. Choi, *J. Chem. Phys.*, 2018, **149**, 104101.

[16] S. Lee, E. E. Kim, H. Nakata, S. Lee and C. H. Choi, *J. Chem. Phys.*, 2019, **150**, 184111.

[17] S. Lee, S. Shotak, M. Filatov and C. H. Choi, *J. Phys. Chem. A*, 2019, **123**, 6455–6462.

[18] Gaussian 16, Revision A.03, M. J. Frisch, G. W. Trucks, H. B. Schlegel, G. E. Scuseria, M. A. Robb, J. R. Cheeseman, G. Scalmani, V. Barone, G. A. Petersson, H. Nakatsuji, X. Li, M. Caricato, A. V. Marenich, J. Bloino, B. G. Janesko, R. Gomperts, B. Mennucci, H. P. Hratchian, J. V. Ortiz, A. F. Izmaylov, J. L. Sonnenberg, D. Williams-Young, F. Ding, F. Lipparini, F. Egidi, J. Goings, B. Peng, A. Petrone, T. Henderson, D. Ranasinghe, V. G. Zakrzewski, J. Gao, N. Rega, G. Zheng, W. Liang, M. Hada, M. Ehara, K. Toyota, R. Fukuda, J. Hasegawa, M. Ishida, T. Nakajima, Y. Honda, O. Kitao, H. Nakai, T. Vreven, K. Throssell, J. A. Montgomery, Jr., J. E. Peralta, F. Ogliaro, M. J. Bearpark, J. J. Heyd, E. N. Brothers, K. N. Kudin, V. N. Staroverov, T. A. Keith, R. Kobayashi, J. Normand, K. Raghavachari, A. P. Rendell, J. C. Burant, S. S. Iyengar, J. Tomasi, M. Cossi, J. M. Millam, M. Klene, C. Adamo, R. Cammi, J. W. Ochterski, R. L. Martin, K. Morokuma, O. Farkas, J. B. Foresman, and D. J. Fox, Gaussian, Inc., Wallingford CT, 2016.

[19] P. Pulay, G. Fogarasi, F. Pang and J. E. Boggs, *J. Am. Chem. Soc.*, 1979, **101**, 2550–2560.

[20] H. B. Schlegel, *J. Comp. Chem.*, 1982, **3**, 214–218.

[21] G. Fogarasi, X. Zhou, P. W. Taylor and P. Pulay, *J. Am. Chem. Soc.*, 1992, **114**, 8191–8201.

[22] P. Pulay, G. Fogarasi, *J. Chem. Phys.*, 1992, **96**, 2856–2860.

[23] J. Baker, *J. Comp. Chem.*, 1993, **14**, 1085–1100.

[24] C. Peng, H. B. Schlegel, *Israel J. Chem.*, 1993, **33**, 449–454.

[25] C. Peng, P. Y. Ayala, H. B. Schlegel, M. J. Frisch, *J. Comp. Chem.*, 1996, **17**, 49–56.

[26] X. Li, M. J. Frisch, *J. Chem. Theory Comput.*, 2006, **2**, 835–839.

[27] H. J. C. Jacobs and E. Havinga, *Adv. Photochem.*, 1979, **11**, 305–373.

[28] R. S. H. Liu and G. S. Hammond, *Proc. Natl. Acad. Sci. U.S.A.*, 2000, **97**, 11153–11158.

[29] S. Grimme, *J. Comput. Chem.*, 2006, **27**, 1787–1799.

[30] A. D. Becke, *J. Chem. Phys.*, 1993, **98**, 5648–5652.

[31] P. J. Stephens, F. J. Devlin, C. F. Chabalowski and M. J. Frisch, *J. Phys. Chem.*, **1994**, **98**, 11623–11627.

[32] J. Tao, J. P. Perdew, V. N. Staroverov and G. E. Scuseria, *Phys. Rev. Lett.*, 2003, **91**, 146401.

[33] Y. Zhao and D. G. Truhlar, *J. Phys. Chem. A*, 2005, **109**, 5656–5667.

[34] Y. Zhao and D. G. Truhlar, *Theor. Chem. Acc.*, 2008, **120**, 215–241.

[35] S. Grimme, S. Ehrlich and L. Goerigk, *J. Comp. Chem.*, 2011, **32**, 1456–1465.

[36] F. Weigend and R. Ahlrichs, *Phys. Chem. Chem. Phys.,* 2005, **7**, 3297–3305.

[37] Y. Yokoyama, T. Iwai, N. Kera, I. Hitomi and Y. Kurita, *Chem. Lett.*, 1990, **19**, 263–264.

[38] Y. Guo, C. Riplinger, U. Becker, D. G. Liakos, Y. Minenkov, L. Cavallo and F. Neese, *J. Chem. Phys.*, 2018, **148**, 011101.

[39] D. G. Liakos, Y. Guo and F. Neese, *J. Phys. Chem. A* 2020, **124**, 90–100.

[40] K. Raghavachari, G. W. Trucks, J. A. Pople and M. Head-Gordon, *Chem. Phys. Lett.* 1989, **157**, 479–483.

[41] F. Neese, *Wiley Interdiscip. Rev. Comput. Mol. Sci.,* 2012, **2**, 73–78.

[42] F. Neese, F. Wennmohs, U. Becker and C. Riplinger, *J. Chem. Phys.*, 2020, **152**, 224108.

[43] E. Papajak, J. Zheng, X. Xu, H. R. Leverentz and D. G. Truhlar, *J. Chem. Theory Comput.,* 2011, **7**, 3027–3034.

[44] L. D. Brown, T. T. Cai and A. DasGupta, *Statist. Sci.,* 2001, **16**, 101–133.

[45] G. Decrouez and A. P. Robinson, *Aust. N. Z. J. Stat.,* 2012, **54**, 281–299.

[46] H. H. Ku, *J. Res. Natl. Inst. Stand. Technol.*, 1966, **70C**, 263–273.